# PARAMETER DEPENDENCE OF EQUILIBRIUM CHARGING POTENTIALS

Paul K. Suh and Michael C. Stauber

Grumman Aerospace Corporation

## ABSTRACT

Equilibrium surface potentials for slab configurations (representative e.g. of a large solar power satellite) are determined under extensive parametric variations of material, solar exposure and substorm characteristics. The results can guide the material selection and design of large space systems to minimize dielectric breakdowns and reduce parasitic leakage currents on SPS.

## INTRODUCTION

Future large space systems, such as a photovoltaic solar power system or a deployable antenna, will be of low-density construction ($\sim 10^{-5}$ g/cm$^3$), employing various light-weight materials. Among the candidate materials being discussed the emphasis is on polymeric materials (Kapton, Teflon, etc) and composites (glass or graphite fibers in an epoxy matrix). Such dielectric materials may be expected to undergo a substantial evolution in their physical properties, including electrical characteristics, as a result of prolonged space environmental exposure. The electrical properties, in particular, may be strongly sensitive to environmental conditions (e.g. temperature), even at the outset, and in some cases (e.g. for composites) remain to be more fully characterized.

This uncertainty and variability in relevant material responses is a major complicating factor in the prediction of spacecraft charging effects for an energetic substorm environment, and provides the major impetus for this paper. Namely, the intent is to explore the consequences for the attained equilibrium charging potentials of systematic variations in such material and exposure related quantities as photoelectric current, electron backscattering yield, secondary electron yield from proton and electron bombardment, material resistivity, and substorm plasma temperature. To identify the impact of such variations in their full context, the analyses include both primary electron and proton currents, together with all their secondary currents, as well as the resistivity-dependent bulk leakage current. The importance of considering resistivity variations can be gauged, for example, from Table 1, in which the bulk resistivity of Kapton and several glasses is seen to change by 4-5 orders of magnitude in traversing the temperature range 25 to 200°C.

The method of analysis utilizes (one-dimensional) Langmuir probe theory, applied to the self-consistent search for the equilibrated surface potential. The geometry employed generally is that of a flat slab, although some exploration is also made of a spherical or cylindrical collection surface. The slab configuration, in particular, is examined under conditions of both single and double sided exposure to the plasma charging currents, with one-sided solar

exposure in some cases. For single-sided plasma exposure, the unexposed side is held uniformly at a reference potential. The case, where the shielded side carries an impressed potential gradient and floats to yield a zero net current to the exposed surface, corresponds to the inner cover slide surface of a solar array and is examined in a companion paper (Paper III-7, this conference).

It is noted that the shadowed slab side exposed to a substorm plasma can develop high negative potentials (tens of kilovolts) that may easily exceed the dielectric breakdown strength of thin sheets (see Table 1). The analyses seek to identify possible adjustments in materials parameters that may prevent such exceedances.

It is also realized that the analysis approach employed has limited validity; in particular it is not adequate for describing conditions near spacecraft edges, nor does it consider the perturbation of particle trajectories that may lead to differential charging. Nonetheless, it is felt that these shortcomings do not seriously distort the influence of the various material responses on the charging process that is explored in this work.

## PLASMA ORIGINATED CURRENTS

The large spacecraft is approximated by an extended slab, and a one-dimensional Maxwell velocity distribution

$$f(v) = \sqrt{\frac{m}{2\pi kT}} \exp\left(-\frac{mv^2}{2kT}\right) \tag{1}$$

is assumed for the substorm plasma particles. The spacecraft surface potential $V_s$ modifies the impinging charged particle distribution.

The incident plasma electron current is thus approximated (Ref. 1) by

$$\begin{aligned} J_e &= J_o \exp\left(-\frac{\varepsilon_s}{kT}\right) \text{ for } V_s < 0 \\ &= J_o\left(1 + \frac{\varepsilon_s}{kT}\right)^g \text{ for } V_s > 0 \end{aligned} \tag{2}$$

where the experimental values for the $J_o$ corresponding to $\sqrt{\frac{kT}{2\pi m}}\, N e$ will be used. Here, $\varepsilon_s = e\,|\,V_s|$, and N and e are, respectively, the electron density and charge. All other notations follow the conventional representation.

The exponential geometric parameter g ranges from 0 for the flat configuration discussed in this paper to 1 for a spherical configuration. Due to the comparatively large Debye length coupled with possible edge effects, the effective g may have a nonvanishing value. Note, however, that the geometric effect can in general be appreciable when $|eV_s|/kT \gtrsim 1$.

For the incident plasma proton current $J_p = \xi J_o$, the experimental value of $\xi \approx 1/40$ is adopted. The $J_p$ augmented by the effect of its secondary electron current $J_{ps} = \phi J_p$ (where $\phi \approx 2.5$ for $V_s < 0$) can become the dominant charging current when the surface potential becomes highly negative. The effect of the surface potential polarity for $J_p$ is opposite to that for electrons as given in Eq. (3).

Adopting the impact yield parameter (Ref. 2) for electrons of energy $\varepsilon_1 = \frac{mV^2}{2}$, i.e.,

$$\delta = \frac{7.4\ \delta m}{\varepsilon_m} (\varepsilon_1 + eV_s) \exp\left[-2\sqrt{\frac{\varepsilon_1 + eV_s}{\varepsilon_m}}\right] \tag{3}$$

that gives the maximum yield $\delta_m$ at energy $\varepsilon_m$, the secondary electron current is approximated by

$$J_s = 2\ J_1\ J_o\ F \tag{4}$$

where $$J_1 = 7.4\ \delta_m\ \frac{kT}{\varepsilon_m} \exp\left(\frac{eV_s}{kT} + \frac{kT}{\varepsilon_m}\right)$$

Values of $\delta_m \approx 3$ and $\varepsilon_m \approx 0.3$ KeV are adopted (Ref. 3) and

$$F = 3!i^3 \sqrt{\frac{\pi}{2}}\ \mathrm{erfc}(y_1) \text{ for } V_s < 0$$

$$= (3!i^3 + (3y_2)2!i^2 + (3y_2^2)i + y_2^3) \sqrt{\frac{\pi}{2}}\ \mathrm{erfc}(y_5) \text{ for } V_s > 0$$

where $y_1 = \sqrt{\frac{kT}{\varepsilon_m}}$, $y_2 = \sqrt{\frac{\varepsilon_s}{kT}}$, and $y_5 = y_1 + y_2$

The backscattered electrons, on the other hand, constitute the high energy portion of the scattered electron spectrum. Since available data here are scant, the following simple approximation, using the backscattering yield parameter $\beta$, is adopted:

$$J_{bs} = \beta J_o \exp\left(-\frac{\varepsilon_s}{kT}\right) \text{ for } V_s < 0$$

$$= \beta J_o \left(1 + \frac{\varepsilon_s}{kT}\right)^{\varepsilon} \exp\left(-\frac{\varepsilon_s}{kT}\right) \text{ for } V_s > 0 \tag{5}$$

This expression often permits separating the backscattering effect out in the analysis, so that a straightforward reassessment of its contribution can be made as more data become available.

The leakage current is approximated by

$$J_\ell = \Delta V_s / R \tag{6}$$

where $R = \rho\ell$ with $\rho$ and $\ell$ representing, respectively the volume resistivity and the slab width. Currents as well as all associated quantities here are given per unit area ($cm^2$).

## PHOTOELECTRON YIELDS IN THE SPACE ENVIRONMENT

The photoelectron yield depends on the material work function and the width and peak of its energy distribution on the solar photon energy spectrum. Spacecraft surfaces in the space environment are, however, quickly contaminated and the surface contamination tends to cause inelastic scattering of the photo-excited electrons (Ref. 4).

The photelectron spectrum from such metals as gold, aluminium, and stainless steel in the space environment was observed to have an energy distribution similar to that for many nonmetals (for example graphite). The photoelectron energy distribution in general has a Gaussian form, peaking at 1~2 eV and tapering off rapidly toward higher energies.

In the absence of a comprehensive theory, on the basis of observed data the photoelectron energy E distribution (normalized to 1) produced by a photon of energy $\omega$ is determined by

$$N(E, \omega) = \frac{2h(\omega)\, E}{1-\exp\left[-h(\omega)(\omega - \varphi)^2\right]} \exp\left[-h(\omega)E^2\right] \tag{7}$$

where $\varphi$ is the work function.

Here $h(\omega) = \dfrac{1}{2E_m^2(\omega)}$, with the approximation

$$E_m(\omega) = E_1\left[1 - \exp\left(\sum_{n=1}^{4} \sigma_n \omega^n\right)\right] \tag{8}$$

for the range of $4.5 < \omega \lesssim 30$ eV. The $E_m(\omega) \to E_1$ toward the upper $\omega$ domain and represents the energy E at which $N(E, \omega)$ peaks.

Values for $\sigma_n$ and $E_1$, derived from empirical data, are

| | Aluminium | Steel | Nonmetal |
|---|---|---|---|
| $\sigma_1$ | $2.84367 \times 10^{-2}$ | $1.45236 \times 10^{-2}$ | 0.292431 |
| $\sigma_2$ | $-1.12782 \times 10^{-2}$ | $2.59762 \times 10^{-3}$ | $-8.82673 \times 10^{-2}$ |
| $\sigma_3$ | $1.32354 \times 10^{-3}$ | $-1.45428 \times 10^{-3}$ | $6.29027 \times 10^{-3}$ |
| $\sigma_4$ | $-7.03183 \times 10^{-5}$ | $3.56235 \times 10^{-5}$ | $-1.59182 \times 10^{-4}$ |
| $E_1$ (eV) | 5 | 2 | 3 |

The photoelectron yield per incident photon of energy $\omega$ is approximated by

$$Y(\omega) = k\omega^p \exp\left(\sum_{n=0}^{4} k_n \omega^n\right) \quad \text{for } 5 \lesssim \omega < 17 \text{ eV}$$
$$= 0.193 \quad \text{for } \omega \gtrsim 17 \text{ eV} \tag{9}$$

where

$k = 2.456 \times 10^6$ $\quad p = -249.874$

$k_1 = 104.388$ $\quad k_2 = -7.20837$

$k_3 = 0.276707$ $\quad k_4 = -4.30132 \times 10^{-3}$

Since the shape of the yields is similar for most of the metal as well as nonmetal cases, as discussed above, any desired adjustment can be made by modifying the parameter k. The photoelectron yield energy distribution is now determined by

$$Y(E, \omega) = Y(\omega)\, N(E,\omega) \tag{10}$$

The continuous and discrete solar photon intensity distributions (in photons/$cm^2$·sec·eV) are approximated by

$$I_{cont}(\omega) = 1.3 \times 10^{19} \exp(-1.985\,\omega) \quad \text{for } 4 < \omega \lesssim 11 \text{ eV}$$
$$= 8 \times 10^9 \quad \text{for } 11 \lesssim \omega \lesssim 15 \text{ eV} \tag{11}$$

$$= 1.2 \times 10^{9} \qquad \text{for } 15 \lesssim \omega < 30 \text{ eV}$$

$$I_{disc} = 2 \times 10^{11} \qquad \text{at } \omega \approx 10.2 \text{ eV}$$

The total photoelectron energy distribution in $(cm^2 \text{ sec eV})^{-1}$ then is

$$Y(E) = \int_{E+\phi}^{\infty} I(\omega)Y(\omega)N(E,\omega)\, d\omega \tag{12}$$

When the spacecraft surface potential $V_s$ is positive, photoelectrons require an energy $E > eV_s$ to overcome the potential barrier. The photoelectron current $\hat{J}_{pe}$ as a function of $V_s$ and with a cut-off at $E \approx 30$ eV, i.e.,

$$\hat{J}_{pe}(V_s) \approx \int_{eV_s}^{30} eY(E)\, dE \tag{13}$$

$$\approx \int eI(\omega)Y(\omega) \frac{\exp[-h(eV_s)^2] - \exp[-h(30-\phi)^2]}{1 - \exp[-h(\omega-\phi)^2]}\, d\omega$$

is shown in Fig. 1. The $\hat{J}_{pe}$ is nearly constant up to 1 eV, beyond which it rapidly becomes negligible as the positive surface potential increases to a few eV.

## MODIFIED SECONDARY ELECTRON YIELD

The emission mechanism for secondary electrons by electron bombardment is similar to the case of photoelectrons. The shapes of the electron energy spectra in both cases are comparable with more than 80% of the secondaries emitted at energies below 20 eV (Ref. 5). As the surface potential turns positive, the secondary electron current thus becomes sensitively dependent on the energy distribution, due to the potential barrier.

Therefore, from Eq. (4), the following simple approximation is adopted for the electron-induced secondary electron energy spectrum,

$$J_{es}(\varepsilon, E) \approx 2J_1 J_o F\, b^2 E \exp(-bE) \tag{14}$$

where $b \approx 0.3\ (eV)^{-1}$ and $\varepsilon = kT$. The integrated secondary electron current modified by positive surface potential $V_s$ is

$$\hat{J}_s(\varepsilon, V_s) \approx 2J_1J_oF \int_{eV_s}^{\varepsilon} b^2 E \exp(-bE)dE \approx J_o\hat{J}_{sec} \quad (15)$$

where, because of $bE \gg 1$,

$$\hat{J}_{sec} \approx 2J_1F(1 + beV_s)\exp(-beV_s)$$

## SURFACE POTENTIAL IN THE DARK

As shown in Fig. 2, a spacecraft in the dark is exposed to a substorm, while its inner surface is maintained at the reference potential zero. The exposed surface in the dark becomes negatively charged, with currents being balanced by

$$J_e = J_p + J_{es} + J_{bs} + J_{ps} + J_\ell \quad (16)$$

Here, as modified by the equilibrium surface potential $V_s$,

$$J_e = J_o \exp\left[-\frac{e|V_s|}{kT}\right] \quad \text{(electron current)}$$

$$J_p = \xi J_o \left[\ldots + \frac{e|V_s|}{kT}\right]^g \quad \text{(proton current)}$$

$$J_{bs} = \beta J_e \quad \text{(backscattering current)}$$

$$J_{es} = J_{so} J_e \quad \text{(electron-induced secondary electron current)}$$

$$J_\ell = \frac{|V_s|}{R} \quad \text{(leakage current)}$$

$$J_{ps} = \phi J_p \quad \text{(proton-induced secondary electron current)}$$

where

$$J_{so} = 7.4\,\delta_m \frac{kT}{\varepsilon_m} \exp\left(\frac{kT}{\varepsilon_m}\right)\sqrt{\pi}3!i^3\operatorname{erfc}\left[\sqrt{\frac{kT}{\varepsilon_m}}\right]$$

and $\phi = 1.5$ is adopted for $V_s < 0$.

Observation indicates that, while the energies of the substorm plasma particles are higher than in quiet periods, their currents are reduced. The substorm electron current (in $nA/cm^2$) adopted in the analysis is approximated (Ref. 6) by

$$J_o = \sum_{n=0}^{4} A_n \varepsilon^n \qquad \text{for } 2 < \varepsilon \lesssim 12 \text{ KeV}$$

$$= 0.5 \qquad \text{for } 12 \text{ Kev} < \varepsilon \tag{17}$$

where $A_o = 2.30725$ $A_1 = -0.255535$

$A_2 = -2.34739 \times 10^{-3}$, $A_3 = 1.79609 \times 10^{-3}$

$A_4 = -7.26494 \times 10^{-5}$, $\varepsilon = kT$

Eq. (16) gives

$$\beta = 1 - J_{so} - \left[ \xi^*\left(1 + \frac{e|V_s|}{kT}\right)^g + \frac{1}{J_o}\frac{|V_s|}{R} \right] \exp\left(\frac{e|V_s|}{kT}\right) \tag{18}$$

where $\xi^* = \xi(1 + \phi)$. In Fig. 3 A and B, respectively for the cases of $g = 0$ and 1, $V_s$ is shown as function of surface potential $\beta$ at various values of electron temperature $\varepsilon = kT$ and resistance R.

At $g = 0$, with a backscattering parameter $\beta = 0.2$, for example $V_s \approx$ (-55, -36, -14, -2) KV at $\varepsilon = 25$ KeV, and $V_s \approx$ (-17, -13, -7, -1.2) KV at $\varepsilon = 10$ KeV, respectively for $R = (\infty, 10^{15}, 10^{14}, 10^{13})$ Ω. The corresponding surface potentials $V_s$ at $g = 1$ with the same backscattering parameter $\beta = 0.2$ are $V_s$ = (-33, -27, -13, -2) KV at $\varepsilon = 25$ KeV and $V_s$ = (-10, -9, -6, -1) KV at $\varepsilon$ = 10 KeV, respectively, for $R = (\infty, 10^{15}, 10^{14}, 10^{13})$ Ω.

At high values of R, there is a large difference in $V_s$ between the cases $g = 0$ and 1, indicating the possible extent of the geometric dependence of $V_s$. For the case of $g = \frac{1}{2}$, the corresponding $V_s$ lies close to the midpoint between the values for $g = 0$ and 1. The high energy tail in the plasma electron distribution helps at high R values to support surface voltages considerably higher than the incident electron temperature (especially in the $g = 0$ case).

The relative magnitude of the various currents (in unit of $J_e$, i.e., $J_i = J_i/J_e$) in the approach to equilibrium is compared in Fig. 4, for example, for the case of $R = 10^{15}$ Ω and $\varepsilon = 15$ KeV. Note that at further higher $V_s$, the initially insignificant $J_p$ and $J_{ps}$ become increasingly important (especially at $g = 1$), eventually overtaking the other $J_i$.

The equilibrium reached at $\Sigma J_i = 1$ for $R = (10^{14}, 10^{15})$ Ω, respectively, yields

$$V_s = (-8.6, -15.5)\ \text{KV} \qquad \text{for } g = 1$$

$$V_s = (-9.7, -22)\ \text{KV} \qquad \text{for } g = 0$$

showing an appreciable dependence of $V_s$ on R and $g$. The strong dependence of $V_s$ on the resistivity is quite significant in view of the fact that R is a sensitive function of temperature (see Table 1) and the surface temperature can undergo large variations.

Also the equilibrium surface potential $V_s$, if it appears across a thin but high resistance material, may become sufficiently high to exceed the dielectric strengths shown in the Table 1. At low R, where the dielectric acts more like a conductor, the leakage current depresses the surface voltage.

Introducing a multiplier I for the plasma electron current

$$J = I\, J_o \tag{19}$$

the effect of current variation on $V_s$ at $R = 10^{15}$ Ω is shown in Fig. 5 for the case of $g = 0$. At low energy, the effect of varying I is small but becomes important at high energies.

## SPACECRAFT POTENTIAL IN THE SUN

As shown in Fig. 6, the spacecraft is exposed to a substorm on the sun illuminated side, while the shadowed side is shielded and held at a reference potential zero. The effective solar intensity is a function of the sun angle θ, causing at large θ a slight modification to the case of spacecraft in the dark discussed previously. The sun exposure at small θ, however, becomes sufficiently strong that the surface potential may become positive.

The low energy electrons (emitted with insufficient vertical velocity) are trapped by the positive potential barrier. Because most of the secondary and photoelectrons are of low energies, a very sensitive balance is established between the surface potential and the currents. The determination of the effective currents ther requires a knowledge of the electron energy distributions.

First, consider the case of $V_s \leq 0$. The surface potential $V_s$ is determined by $J_o - J_{os} - J_p - J_g - J_{pe} - J_{bs} - J_{ps} = 0$, yielding

$$\beta \approx 1 - J_{so} - \left[\xi^* \left(1 + \frac{e V_s}{kT}\right)\beta + \frac{1}{J_o}\frac{|V_s|}{R} + \frac{J_{pe}}{J_o}\right] \exp\left(\frac{e|V_s|}{kT}\right) \qquad (20)$$

For $V_s = 0$, Eq. (20) is reduced, with $\Sigma = 1 - J_{so} - \xi^*$, to

$$\Sigma - \left(\beta + \frac{J_{pe}}{J_o}\right) = 0 \qquad (21)$$

requiring $\Sigma - (\beta + J_{pe}/J_o) \gtrless 0$ for $V_s \lessgtr 0$. Since the $\Sigma$ (shown in Fig. 7) is independent of $J_o$, $\xi$ and R, Eq. (21) itself is independent of g and R.

Since $\Sigma \approx 0.74$ at $\varepsilon = 25$ KeV and 0.49, at $\varepsilon = 10$ KeV, for example (with the backscattering parameter $\beta = 0.2$)

$$J_{pe}/J_o \lesssim 0.54 \text{ at } \varepsilon = 25 \text{ KeV}$$

$$\lesssim 0.29 \text{ at } \varepsilon = 10 \text{ KeV}$$

are required for $V_s \lesssim 0$. With substorm currents $J_o \approx 0.5$ and 0.58 $nA/cm^2$, respectively, at $\varepsilon = 25$ and 10 KeV,

$$J_{pe} > 0.27 \text{ nA/cm}^2 \text{ at } \varepsilon = 25 \text{ KeV}$$

$$> 0.17 \text{ nA/cm}^2 \text{ at } \varepsilon = 10 \text{ KeV}$$

to charge the spacecraft surface positive.

For the case of $V_s < 0$, the equilibrium surface potential $V_s$ at $R = 10^{15}$ $\Omega$ is plotted in Figs. 8A and B as a function of backscattering yield $\beta$ for $\varepsilon = 25$ and 15 KeV, by varying $J_{pe}$ (in $nA/cm^2$ at $V_s = 0$). The solid lines here are for the substorm currents $J_o$ of Eq. (17), while the dashed lines are for the doubled substorm current $2J_o$ case [see Eq. (9)].

For $R = 10^{15}$ $\Omega$, there is an appreciable shift in the $\beta - V_s$ curves in going from $\xi = 1$ to $\xi = 0$ (i.e., from a sphere to an infinite plane), both at $\varepsilon = 25$ KeV (Fig. 8A) and 15 KeV (Fig. 8B). At $\varepsilon \lesssim 5$ KeV for $R = 10^{15}$ $\Omega$, as well as at $R \lesssim 10^{14}$ for all electron temperatures, however, the shift generally becomes

negligible. For $R \lesssim 10^{11}$ Ω, the surface potential $V_s$ readily turns positive.

For a given R, the effective β as function of $V_s$ gradually becomes smaller as ε is reduced. For small $J_{pe}$ ($\lesssim 0.1$ nA/cm$^2$), there is substantial latitude for β to keep $V_s$ negative, especially when ε is high. As $J_{pe}$ increases beyond a few tenths of nA/cm$^2$, however, $V_s$ is likely to turn positive. The $\beta - V_s$ curves rapidly reach a plateau as $|V_s|$ decreases, making the determination of the surface potential as function of β there delicate.

Relative strength of the currents at ε = 15 KeV and $J_{pe}$ = 0.01 nA/cm$^2$ in units of $J_e = J_o \exp(- e|V_s|/kT)$, i.e.,

$$j_i = J_i/J_e$$

are shown in Figs. 9A and B, respectively, for $R = 10^{15}$ and $10^{13}$Ω. Note that, especially at $R = 10^{15}$ Ω, all currents are in the same order of magnitude near equilibrium [By coincidence, $j_{pe} \approx j_p(g = 0)$ here].

The shifts in $j_p(g)$ and $j_{ps}(g)$ between the g = 1 and 0 cases are appreciable for $R \simeq 10^{15}$ Ω. For $R \lesssim 10^{13}$, the difference in the currents between the g = 1 and 0 cases is small and thus ignored in the diagram.

For $R \gtrsim R_c = O(10^{17}$ Ω), the effect of $J_\ell$ is negligible and the material behaves as a perfect insulator (i.e., R = ∞). For $R < R_c$, $J_\ell$ increases steeply toward the equilibrium $V_s$, and, especially when β is low, $J_\ell$ becomes significant even at relatively high R. For $R < O(10^9$ Ω), the material practically behaves as a conductor.

When $V_s > 0$, while the primary plasma electrons are accelerated toward the spacecraft, the emitted electrons are retarded by the potential barrier. Because of the low energy of the secondary and photoelectrons, the balancing of the various currents for the positive $V_s$ by

$$J_e + J_\ell - \hat{J}_{pe} - \hat{J}_{es} - J_p - \hat{J}_{bs} - \hat{J}_{ps} = 0 \qquad (22)$$

becomes delicate. Here, $\hat{J}_{pe}$ and $\hat{J}_s$ are given, respectively, in Eqs. (13) and (15), and $\hat{J}_{ps}$ corresponds to $\hat{J}_{es}$ (and $\hat{J}_{bs}$).

Solar incidence here is assumed to be nearly vertical, and the photoelectric current is normalized to approximately 1.5 nA/cm$^2$ at zero surface potential.

Reduction of the solar intensity with an increased sun-angle may cause the spacecraft to become negatively charged, as discussed above. Because of $|eV_s|/kT \ll 1$ here, possible geometric effects in the electron attraction to the surface are negligible.

For $R = 10^9$ Ω, the $J_\ell$ becomes significant and increases rapidly with $V_s$. The equilibrium surface potentials are thus small ($V_s = 0.92$ V and 0.8 V at KT = 15 KeV, respectively, for the I = 1 and 2 cases), and, in approaching equilibrium, the currents other than $J_\ell$ are nearly constant.

At low R, the $J_\ell$ thus becomes the controlling factor in the determination of $V_s$. The effective $V_s$ as a function of ε and R are shown in Fig. 10, again with $\beta = 0.2$ and $J_{pe}(V_s = 0) = 1.5$ nA/cm$^2$ (the solid and dotted lines are, respectively, for the I = 1 and 2).

The $V_s$ is not much affected by the variation of R from $10^{11}$ to $10^{15}$ Ω. Below $10^{10}$ Ω, however, decreases in R give rise to a progressively stronger reduction in the effective $V_s$. Note also that as expected, the $V_s$ for a given R is a decreasing function of average plasma electron energy ε, although the dependence is relatively weak.

## SPACECRAFT TOTALLY IMMERSED IN A SUBSTORM

The case of a slab configuration spacecraft totally immersed in a substorm environment in the earth's shadow is similar to that of a spacecraft slab of infinite resistance unilaterally exposed to the substorm in the dark. With sun exposure on one side (see Fig. 11), however, a potential difference develops between the two surfaces.

If the incident solar intensity is weak, due to a large sun angle $\theta$, the two surface potentials $V_1$ and $V_2$ remain negative. When the solar exposure becomes sufficiently strong, the illuminated side potential $V_1$ turns positive, while the dark side potential $V_2$ remains negative at large values of the bulk resistance R but eventually may turn positive for small R. The potential difference between the two surfaces induces a leakage current $J_\ell$.

First, consider the case of $V_{1,2} \leq 0$, by writing

$$M_{1,2} = - V_{1,2} \tag{23}$$

The explicit current balance equations to be simultaneously solved are

$$\frac{M_1 - M_2}{RJ_o} + \left[ \eta \exp\left(-\frac{eM_2}{kT}\right) - \xi^*\left(1 + \frac{eM_2}{kT}\right)^g \right] = 0 \tag{24}$$

$$\frac{J_{pe}}{J_o} + \xi^* \left[\left(1 + \frac{eM_1}{kT}\right)^g + \left(1 + \frac{eM_2}{kT}\right)^g \right] - \eta \left[\exp\left(- \frac{eM_1}{kT}\right) + \exp\left(- \frac{eM_2}{kT}\right)\right] = 0$$

where $\eta = 1 - \beta - J_{so}$, $\xi^* = \xi(1 + \phi)$, and g is the geometric configuration parameter.

For the case of $M_1 = 0$, the above relations are simplified to

$$\frac{M_2}{R} = J_o \left[ \eta \exp\left(- \frac{eM_2}{kT}\right) - \xi^*\left(1 + \frac{eM_2}{kT}\right)^g \right] \tag{25A}$$

$$(J_{pe})_c = \frac{M_2}{R} + J_o(\eta - \xi^*) \tag{25B}$$

Note that $(J_{pe})_c$ is the value of $J_{pe}$ needed to raise the surface potential $V_1$ to zero.

The $M_2$ is determined by solving Eq. (25A) as function of $\epsilon = kT$, and the results are shown in Fig. 12 for the cases of various values of R and $\beta = 0.2$. The corresponding critical photoelectric current $(J_{pe})_c$ is in turn determined by Eq. (25B) as shown in Fig. 13. The impact of the geometric parameter variation from $g_2 = 1$ to 0 is generally negligible with low R but becomes noticable for $R \gtrsim 10^{15}$ Ω as shown in Fig 13 and especially in Fig. 12.

When $eM_2/kT \ll 1$, Eq. (25A) is reduced to

$$M_2 \approx (\eta - \xi^*) / \left[\frac{1}{RJ_o} + e(\eta + g\xi^*)/kT \right] \tag{26}$$

The relation is further simplified for $(RJ_o)^{-1} \gg e(\eta + \xi^*)/kT$ to

$$M_1 \approx RJ_o(\eta - \xi^*) \tag{27}$$

where $M_1$ now becomes proportional to R.

The $\eta$ is independent of R but is a function of $\epsilon$ and approaches $\xi^* \approx 0.07$ toward $\epsilon \approx 5.3$ KeV. Therefore, $M_o$ in Fig. 12 vanishes rapidly as $\epsilon$ decreases toward 5.3 KeV. In Fig. 13, $(J_{pe})_c$ is seen to approach rapidly a limiting value as R decreases to the order of $10^{11}$ Ω (where the approximation (27) becomes good) and also to decrease steeply toward $\epsilon \approx 5.3$ KeV. This characteristic is expected, because the $(J_{pe})_c$ determined there by Eq. (25B) becomes (in conjunction with (27)) proportional to $\eta - \xi^*$ and independent of R.

As the unmodified $J_{pe}$ exceeds $(J_{pe})_c$, the sun exposed side becomes positive. The low energy electrons in the secondary and particularly in the photoelectric currents on this side are then trapped by the potential barrier as discussed previously.

While $V_{1,2} < 0$, the Eqs. (24) are solved for the surface potential $M_{1,2} = -V_{1,2}$, with its corresponding leakage current $J_\ell = (M_2 - M_1)/R$. When the sun exposed side becomes positively charged (i.e., $V_1 = M_1 > 0$), while the shadowed side remains negatively charged, (i.e., $V_2 = -M_2 < 0$), the corresponding equations become

$$\frac{M_1 + M_2}{R} = \hat{J}_{pe} + \hat{J}_{es} + \hat{J}_{bs} + J_o\left[\xi^* \exp\left(-\frac{eM_1}{2kT}\right) - \left(1 + \frac{eM_1}{kT}\right)\xi\right]$$
$$= J_o\left[\eta \exp\left(-\frac{eM_2}{kT}\right) - \xi^*\left(1 + \frac{eM_2}{kT}\right)\xi\right] \tag{28}$$

Here, because of the relative smallness of $J_p$ on the sun exposed side (which is at a very low positive surface potential), a simple approximation of $\xi \approx \xi^*$ is adopted. The integrated $\hat{J}_{pe}$ and $\hat{J}_{es}$ are given, respectively, in Eqs. (14) and (15).

The $V_{1,2}$ as function of $J_{pe}(V_s = 0)$ are shown in Figs. 14A and B, respectively, for the cases of $R = 10^{15}$ and $10^{10}$ Ω, with $\beta = 0.2$. For $R \leq 10^{11}$ Ω, $V_1 \approx V_2$ in the domain of $J_{pe}(V_s = 0)$ where $V_1 < 0$.

The effect of changing the geometric parameter g from 1 to 0 is apparent only when $|eV_s|/kT$ is comparatively large, as seen from the figures. Note, however, that as $V_1$ rapidly turns positive while leaving the magnitude of the negative $V_2$ large, the resulting large potential difference between the two surfaces produces a correspondingly large leakage current $J_\ell$. This large $J_\ell$ then negates the relative importance of the effect of the shifts in $J_p$ and $J_{ps}$ due to the variation in g, even if $|eV_s|/kT$ is not small.

For $J_{pe} = 0$, $V_1 = V_2 < 0$, which, as stated above, corresponds to the surface potential of an isolated (i.e., $R \to \infty$) spacecraft slab unilaterally exposed to the substorm in the dark (see previous section and Figs. 3A and B). As $J_{pe}$ increases, $V_1$ rises rapidly to become positive at $(J_{pe})_c$ (see Fig. 14) and quickly reaches a plateau value of a few to several volts.

This is due to the low energy of the secondary and especially photoelectrons, resulting in a rapid increase in the current attenuation when the surface potential turns positive and begins to rise.

The value of the bulk resistance R primarily affects $V_2$. For $R = 10^{15}$ Ω, because the leakage current $J_\ell$ is relatively small, $V_2$ remains essentially the same throughout the variation of $J_{pe}(V_s = 0)$, while $V_1$ increases rapidly and turns to stabilize at a small positive value.

When R is reduced to $10^{10}$ Ω, because of the large leakage current $J_\ell$, $V_1$ increases and turns positive at relatively slower rate than for $R = 10^{15}$ Ω, while $V_2$ keeps increasing and may change sign to become positive, especially in the low ε domain.

For a given $J_{pe}(V_s = 0)$, $V_1$ and $V_2$ are, respectively, an increasing and decreasing function of R, while both $V_{1,2}$ are decreasing functions of $J_o$. In a typical substorm environment, the sun exposure may turn both $V_{1,2}$ positive for $\varepsilon < 5.3$ KeV and (in general) $R < 10^{10}$ Ω. The positive excursion of $V_1$ and $V_2$ is restricted to a few volts.

## SUMMARY AND CONCLUSIONS

The primary objective of this paper has been to describe the dependence of the charging process for dielectric surfaces on the various material response characteristics. This was done with the intent of exhibiting the ranges of magnitudes over which certain materials parameters either have a significant influence on the charging process or contribute only weakly to the charging levels attained. For this purpose it was important to include in the analysis all the currents involved in the equilibration of the charging potential. Where possible the material dependence of these currents was described by variables to facilitate parametric excursions. The main areas treated in the analyses and the chief conclusions derivable from the results are as follows:

The influence of bulk resistance on the charging potential was analyzed parametrically for $R \gtrsim 10^{10}$. The results show that for the lowest part of this resistance range the leakage current becomes a dominant factor in the equilibration process. For high resistance values the shadowed side of a dielectric slab in a substorm environment can develop a large negative potential. In this case the otherwise relatively insignificant plasma proton current and its secondary electron current may assume a dominant role in preventing further growth of the negative potential. In view of the conspicuous dependence of equilibrium potentials on dielectric resistivities, the large variability of resistivity values for important candidate materials makes the prediction of charging potentials problematic. Also, for dielectric materials of a few mils thickness, such as Kapton sheets, the potential differences developed are frequently sufficient to produce dielectric breakdown. Repeated breakdown in turn may lead to progressive changes in resistivity.

For a sheet of dielectric material the equilibrium potential $V_s$ on the sun-illuminated side tends to saturate for $J_{pe} \sim 1$ nA/cm$^2$. The saturation $V_s$ is a few volts positive and depends only weakly on kT. The largest effect on $V_s$ is in the range 0 - 0.5 nA/cm$^2$, where $V_s$ moves from large negative (kV) values to small positive values. This dynamic behavior is important in sun-angle variations and terminator crossings. If the bulk resistance of the sheet is large, the shadowed side potential settles at a large negative value; however, for a sufficiently low resistance ($\sim 10^{10}$ ohm-cm$^2$) both sides may become positive.

An analysis of the sensitivity of the charging process to the value of the backscattering yield $\beta$ shows the following trend: If $\beta$ is significantly larger than 0.2, then at lower substorm plasma temperatures (e.g. $kT \lesssim 5$ keV), even a shadowed surface may turn positive. However, for large kT (> 10 keV) the influence of $\beta$ on the attained surface potential $V_s$ becomes progressively weaker.

## REFERENCES


1. Langmuir, I. and Mott-Smith, H. M. (1920), Phys. Rev., vol. 28, no. 717.

2. Sternglass, E.J., Phys. Rev., vol. 80, p. 925, 1950.

3. Willis, R.F. and Skinner, D.K., Solid State Communications, vol. 13, p. 685, 1973.

4. Feuerbacher, B. and Fitton, B (1972), J. Appl. Phys. vol. 43, no 15, p. 15, 1972.

5. Grad, R.J.L, Knott, K, and Pedersen, A., Photon and Particle Interactions with Surfaces in Space, D. Reidel Pub. Co., Dordrecht-Holland; 1972.

6. Stevens, N.J., Lovell, R.R., and Purvis, C.K., Proc. of the Spacecraft Charging Technology Conf., vol. 735, 1977.


**Table 1 Electrical Characteristics of Selected Dielectrics**

| | VOLUME RESISTIVITY (Ω-CM) | DIELECTRIC STRENGTH (VOLTS/MIL) |
|---|---|---|
| TEFLON FEP | $10^{18}$ (25-175°C) | $8\cdot10^{3}$ (0.5 MIL) – $4\cdot10^{3}$ (4 MIL) |
| KAPTON | $10^{18}$ (25°C) – $10^{14}$ (200°C) | $7\cdot10^{3}$ (1 MIL) – $4.6\cdot10^{3}$ (3 MIL) |
| BOROSILICATE GLASS | $5\cdot10^{13}$ (25°C) – $5\cdot10^{9}$ (200°C) | $1\cdot10^{4}$ – $2\cdot10^{4}$ |
| FUSED SILICA | $10^{18}$ (25°C) – $5\cdot10^{13}$ (200°C) | $1\cdot10^{4}$ – $2\cdot10^{4}$ |
| SODA LIME GLASS | $10^{11}$ (25°C) – $5\cdot10^{7}$ (200°C) | $1\cdot10^{4}$ – $2\cdot10^{4}$ |

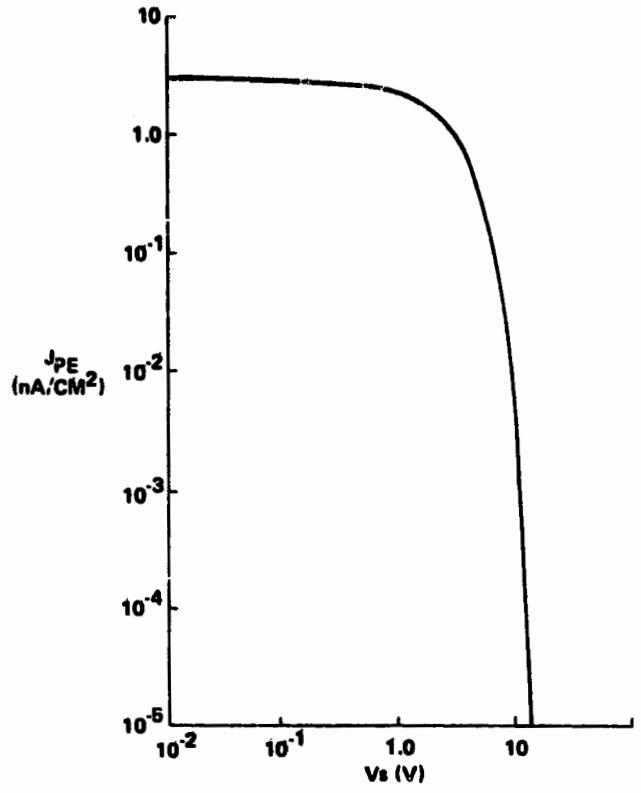


1003-78/82-1

**Fig. 1 Attenuation of Integrated Photoelectric Current by Positive Surface Potential Barrier $V_S$**

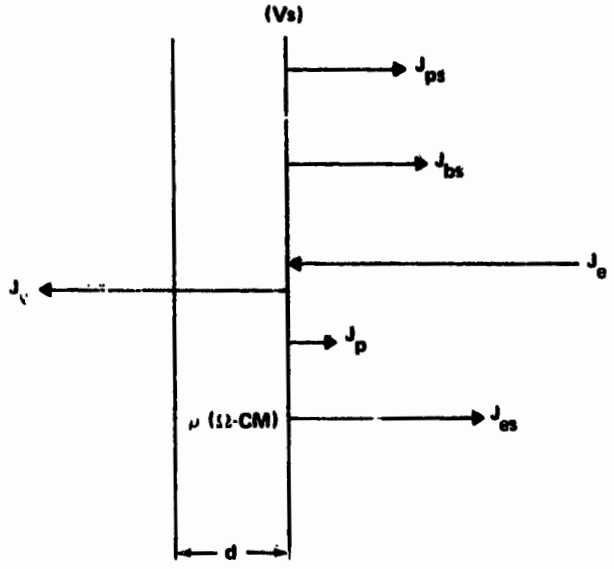


**Fig. 2 Substorm Plasma Generated Charging Currents Under Eclipse Conditions**

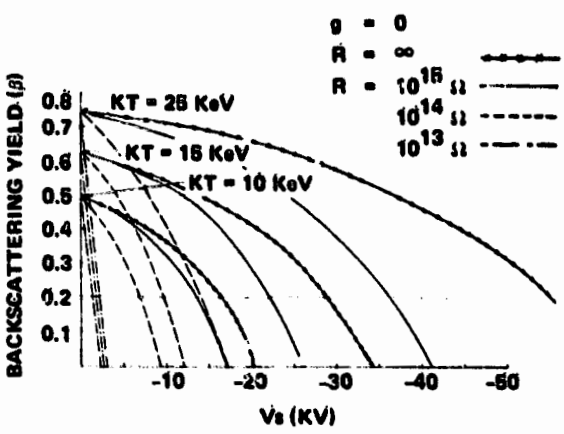


Fig. 3A Effect of Backscattering Yield and Leakage Currents on Equilibrium Surface Charging Potential for Infinite Flat Surface (Typical Substorm Currents in Eclipse)

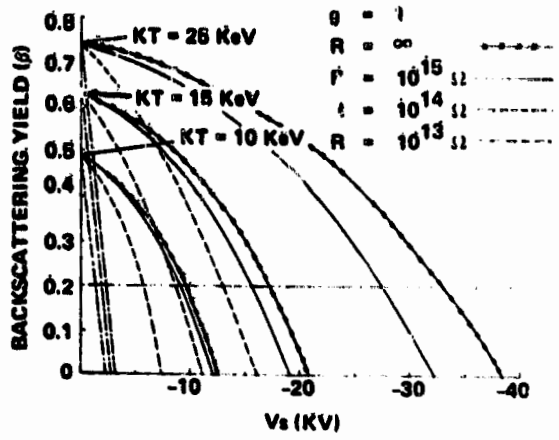


Fig. 3B Effect of Backscattering Yield and Leakage Currents on Equilibrium Charging Potential for Spherical Surface (Typical Substorm Currents in Eclipse)

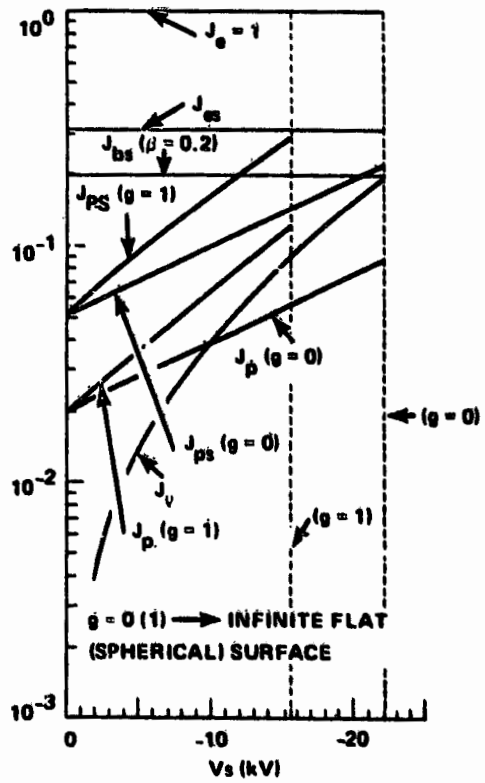


Fig. 4 Surface Potential Dependence of Various Charging Currents in the Dark (Relative to je = 1) in Approach to Equilibrium ($R = 10^{15}$ Ω, kT = 15 KeV)

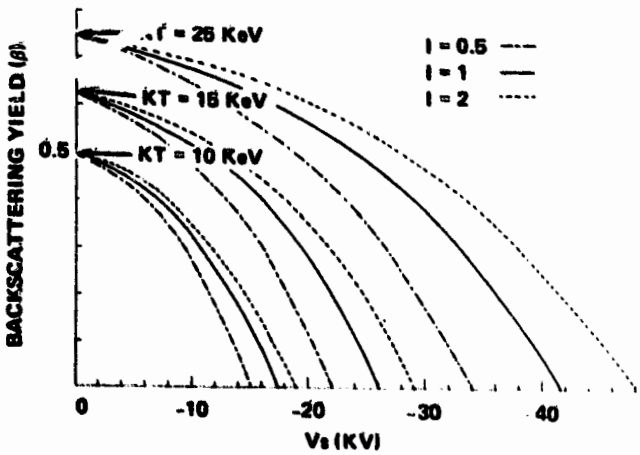


Fig. 5 The Equilibrium Surface Potential Vs as Function of the Backscattering Yield β for Various Current Multiplyer l and Electron Temperature kT (g = 0 Case at $R = 10^{15}$ Ω)

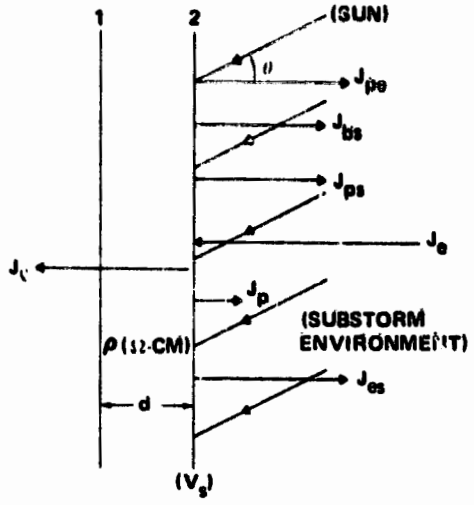


Fig. 6 Plasma Charging Current and Secondary Currents on a Sun-Illuminated Surface (2) (Interior Surface (1) at Reference Potential)

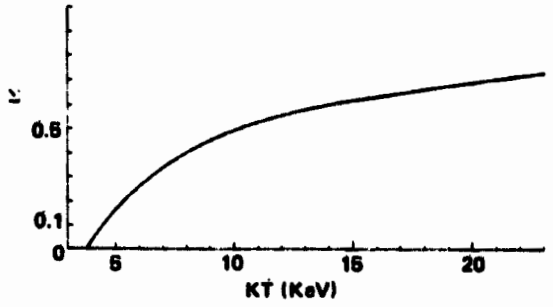


Fig. 7 Effect of Combined Backscattering/Photo-Electric Current at Zero Surface Potential on Polarity of Equilibrium Charging Potential $(\Sigma - (\beta + J_{pe}(0)/J_e(0)) \gtrless 0 \rightarrow V_s \lesssim 0)$

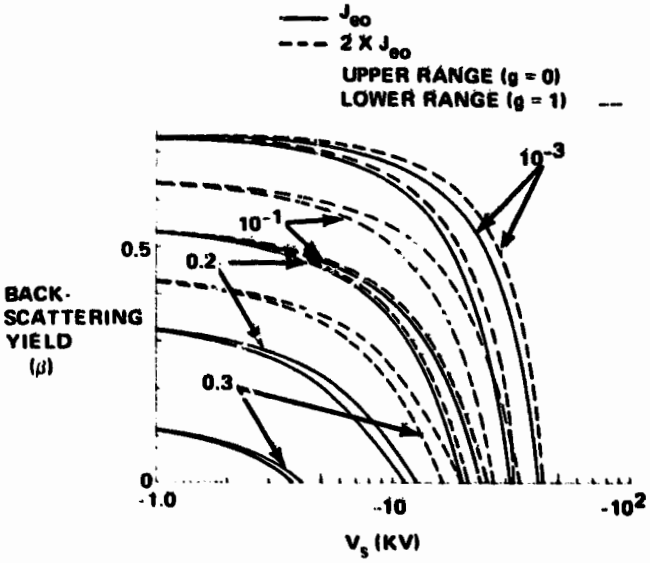


Fig. 8A Surface Charging Potential as Function of Backscattering Yield β for Various $J_{pe}$ ($V_s$ = 0) Values Appropriate to Large Sun Angles (kT = 25 keV; R = $10^{15}$ Ω)

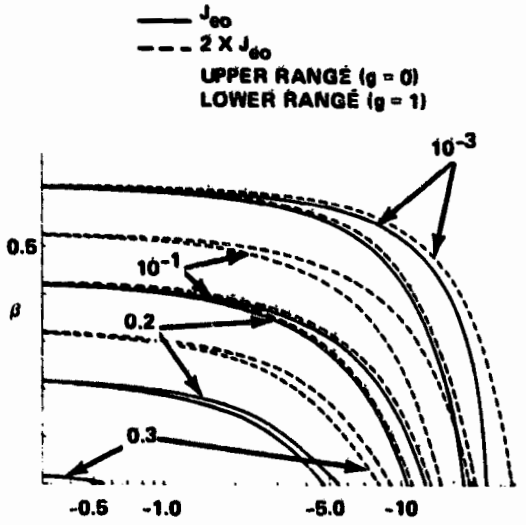


Fig. 8B Surface Charging Potential as Function of Backscattering Yield β for Various $J_{pe}$ ($V_s$ = 0) Values Appropriate to Large Sun Angles (kT = 15 keV; R = $10^{15}$ Ω)

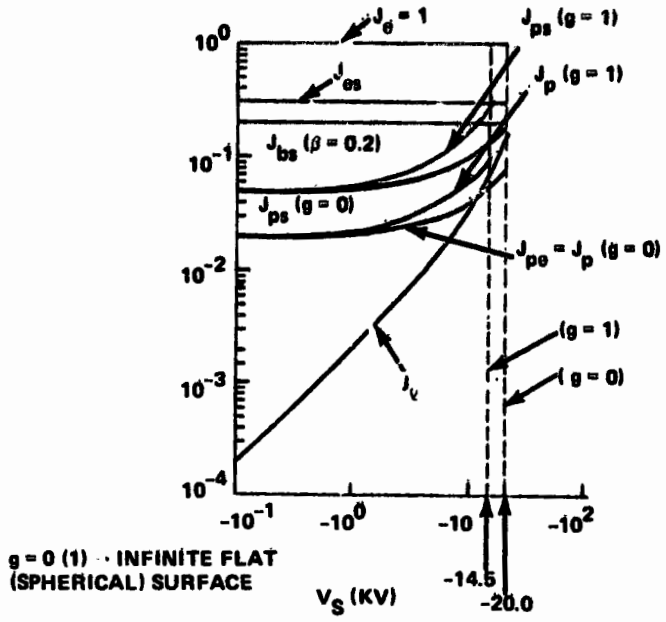


Fig. 9A Surface Potential Dependence of Various Charging Currents (Relative to $J_e = 1$) in Approach to Equilibrium ($R = 10^{15}\ \Omega$; kT = 15 KeV; $\beta = 0.2$; $J_{pe}$ ($V_s = 0$) = 0.01 nA/cm$^2$)

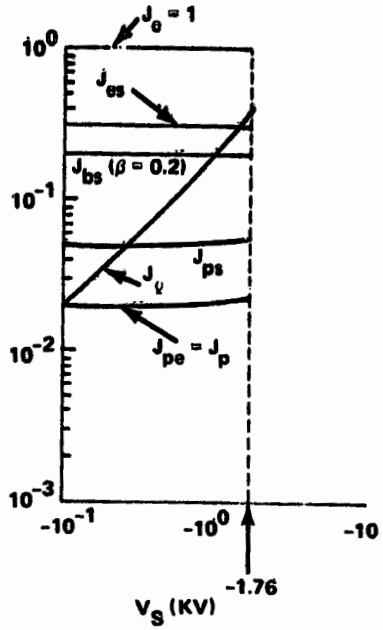


Fig. 9B Surface Potential Dependence of Various Charging Currents (Relative to $J_e = 1$) in Approach to Equilibrium ($R = 10^{13}\ \Omega$; kT = 15 KeV; $\beta = 0.2$; $J_{pe}$ ($V_s = 0$) = 0.01 nA/cm$^2$)

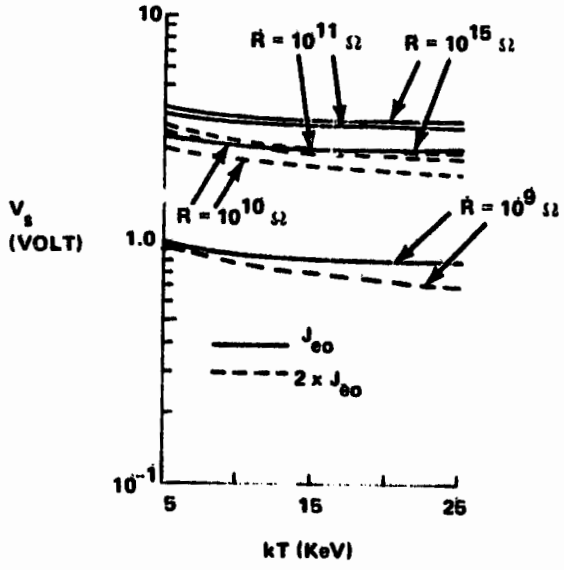


Fig. 10 Positive Surface Potential $V_s$ As Function of Average Plasma Electron Energy kT and Resistance R. ($J_{pe}$ ($V_s = 0$) = 1.5 nA/cm$^2$)

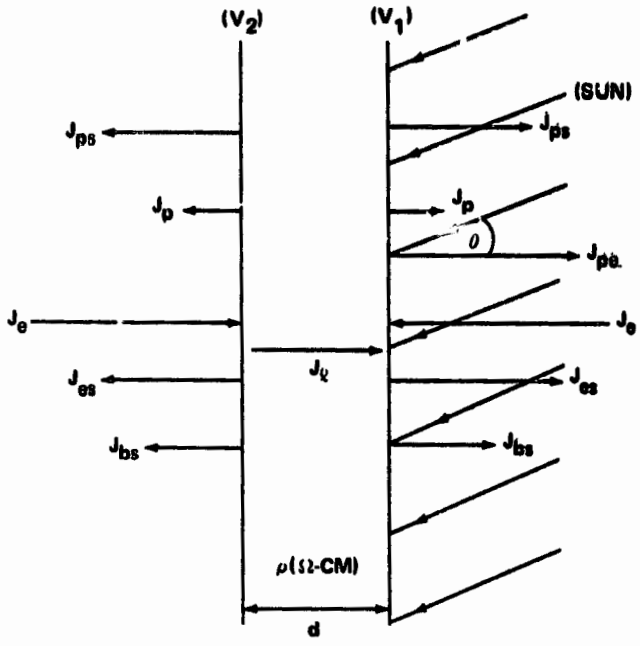


Fig. 11 Plasma Charging Currents and Secondary Currents on Substorm Environment Immersed Slab (One Side Sun-Illuminated)

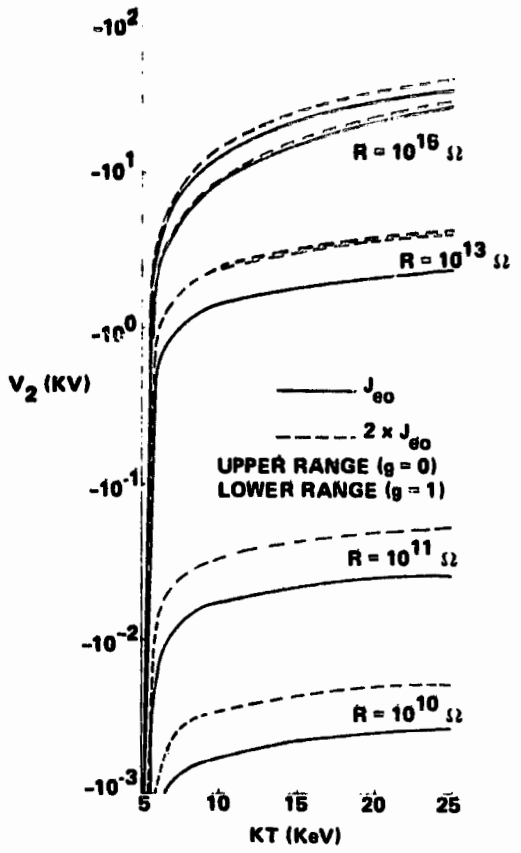


Fig. 12 Shadowed Side Surface Potential $V_2$ for Sun-Illuminated Side Potential $V_1$ = 0, as Function of Resistance and Electron Temperature (Backscattering Yield $\beta$ = 0.2)

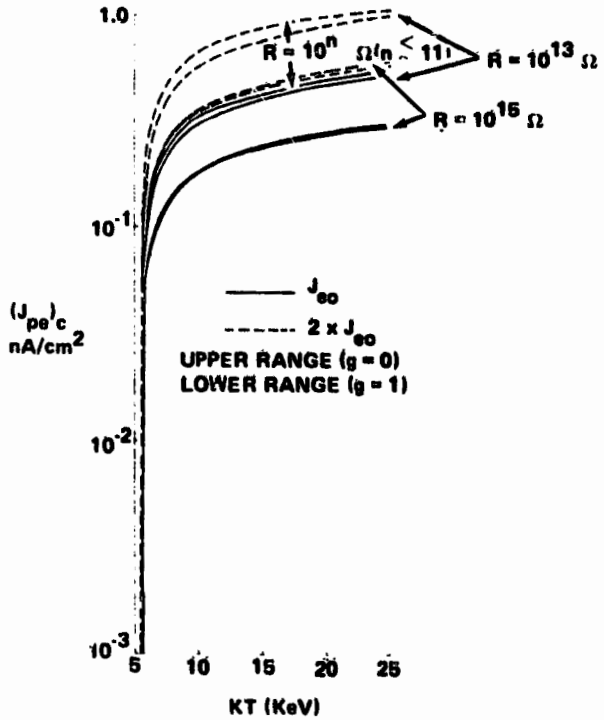


Fig. 13 The Critical Photoelectric Current $(J_{pe})_c$ for Sun-Illuminated Side Potential $V_1$ = 0, as Function of Resistance and Electron Temperature (Backscattering Yield $\beta$ = 0.2)

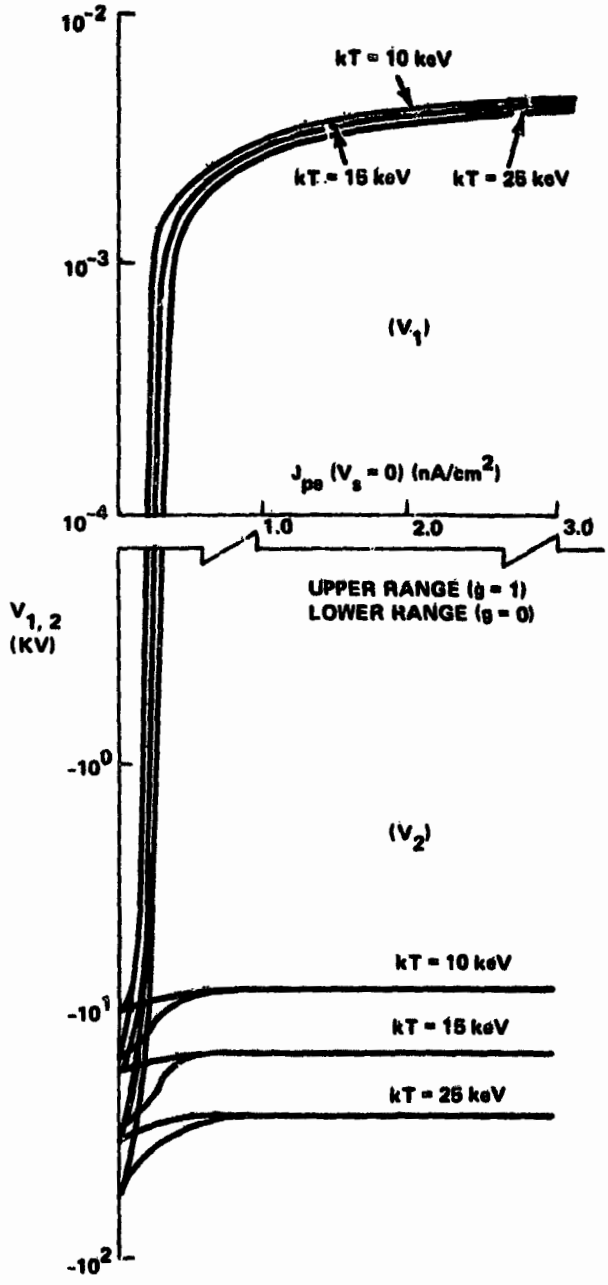


Fig. 14A Equilibrium Charging Potentials on Slab Immersed in Substorm Environment (One Side Sun-Illuminated) as Function of $J_{pe}$ $(V_S = 0)$ $(R \sim 10^{15}\ \Omega; \beta = 0.2)$

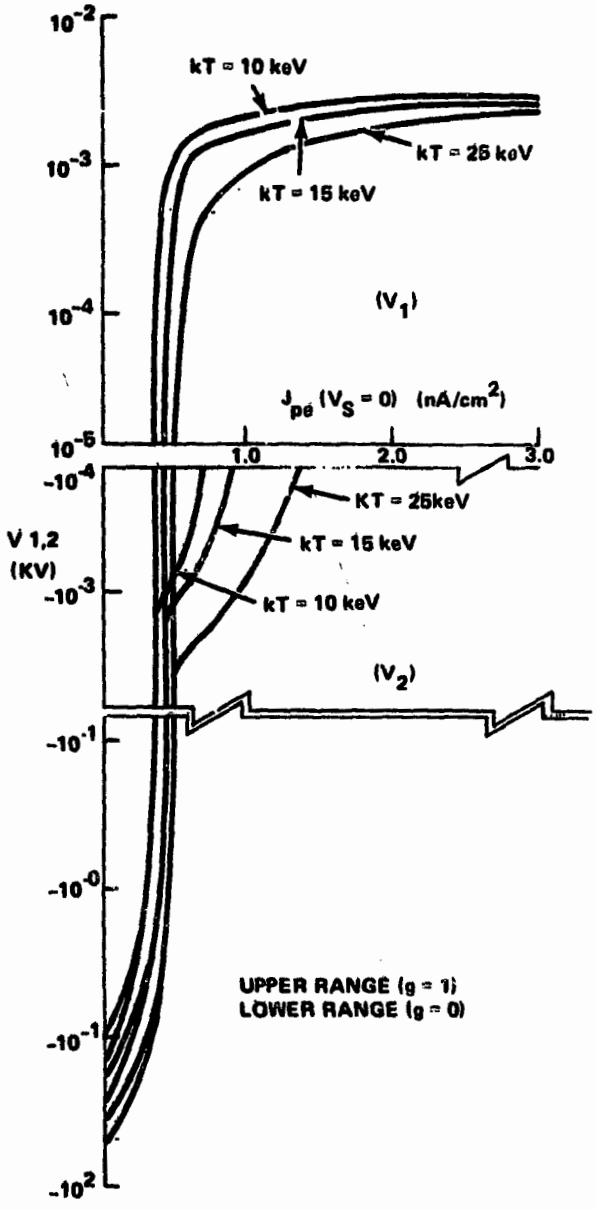


Fig. 14B Equilibrium Charging Potentials on Slab Immersed in Substorm Environment (One Side Sun-Illuminated) as Function of $J_{pe}$ $(V_S = 0)$ $(R = 10^{10}\ \Omega; \beta = 0.2)$